HHS Public Access

Author manuscript

Magn Reson Med. Author manuscript; available in PMC 2017 September 15.

Published in final edited form as:

Magn Reson Med. 2010 September ; 64(3): 902–906. doi:10.1002/mrm.22452.

Manganese-Enhanced MRI of Salivary Glands and Head and Neck Tumors in Living Subjects

Mukund Seshadri[1,2,3,*] and **Allison Hoy**[4]

[1]Preclinical Imaging Facility, Roswell Park Cancer Institute, Buffalo, NY, USA

[2]Cancer Biology, Roswell Park Cancer Institute, Buffalo, NY, USA

[3]Dentistry and Maxillofacial Prosthetics, Roswell Park Cancer Institute, Buffalo, NY, USA

[4]State University of New York–University at Buffalo School of Medicine, Buffalo, NY, USA

Abstract

Manganese-enhanced MRI has previously been used for visualization of brain architecture and functional mapping of neural pathways. The present work investigated the potential of manganese-enhanced MRI for noninvasive imaging of salivary glands in living subjects. Marked shortening of T_1 was observed in salivary glands of naïve mice ($n = 5$) 24–48 h after systemic administration of $MnCl_2$ (0.4 mmol/kg, intraperitoneally). Three-dimensional MR microscopy confirmed selective contrast enhancement of salivary gland tissues post–$MnCl_2$ injection. Ectopic and orthotopic head and neck tumor xenografts also showed an increase in R_1 at 24 h following $MnCl_2$ injection (0.2 mmol/kg, intraperitoneally). However, tumor enhancement was minimal compared to salivary gland tissue. Salivary gland R_1 values were lower in mice bearing orthotopic head and neck tumors compared to naïve mice. These results demonstrate, for the first time, the usefulness of manganese-enhanced MRI in the visualization of salivary glands and head and neck tumors in vivo.

Keywords

salivary glands; ME-MRI; manganese chloride; T_1-relaxation; head and neck tumors

The potent paramagnetic effects of manganese ions (Mn^{2+}) have led to its extensive investigation as an MR contrast agent for several decades now (1–3). Early studies determined the relaxation effects of manganese in tissues (3) and successfully demonstrated the utility of Mn^{2+} in providing quantitative estimates of water exchange in erythrocytes (4). Since then, manganese has been used as a contrast agent for MR imaging in experimental model systems for multiple biologic applications (5). Published studies have focused on the use of Mn^{2+} as a contrast-enhancing agent (6) or as a marker of calcium influx in tissues (7). Studies have also demonstrated the usefulness of manganese-enhanced MRI (ME-MRI) for functional brain mapping (8) and visualization of neural and auditory pathways (9,10). ME-MRI has also been successfully used for imaging cardiac function and ischemic areas in the

*Correspondence to: Mukund Seshadri, BDS, PhD, Cancer Cell Center, Rm 164, Roswell Park Cancer Institute, Elm and Carlton Streets, Buffalo, NY 14263. mukund.seshadri@roswellpark.org.

myocardium (11). However, the utility of ME-MRI in visualizing salivary glands has not been reported.

The aim of the present study was to determine if ME-MRI could be applied for visualization of salivary gland tissues in vivo. Enhancement characteristics of salivary glands were studied in nude mice following systemic administration of $MnCl_2$. Quantitative measure of contrast enhancement was obtained by measuring the T_1-relaxation rate ($R_1 = 1/T_1$) of salivary gland tissues in naïve animals before and at different times after administration of $MnCl_2$. T_1 mapping of salivary gland tissue and ME-MR microscopy were performed 24 h after administration of $MnCl_2$. T_1-weighted ME-MRI was applied to image subcutaneous human head and neck squamous cell carcinoma (HNSCC) xenografts. ME-MRI of salivary glands was also performed in mice bearing orthotopic head and neck squamous cell carcinomas to demonstrate the usefulness of the technique in simultaneous imaging of tumor and salivary gland tissues.

MATERIALS AND METHODS

Animals, $MnCl_2$ Administration, and Study Design

Twenty-seven female athymic nude mice (12–15 weeks of age, 20–25 g body weight; Harlan Laboratories, Indianapolis, IN) were used for experimental imaging studies. Animals were kept in microisolator cages in a laminar flow unit under ambient light, with free access to food and water. Imaging studies were carried out using naïve (non-tumor-bearing) and tumor-bearing animals. Ectopic and orthotopic human HNSCC xenografts were establishing by injecting 1×10^6 FaDu cells into mice either subcutaneously in the lower flanks (ectopic) or transcervically into the floor of the mouth (orthotopic) as described previously (12). Studies were performed in accordance with protocols approved by the Institutional Animal Care and Use Committee. A 40-mM stock solution of $MnCl_2$ in saline was prepared and animals injected at a dose of 0.2 or 0.4 mmol/kg by intraperitoneal (i.p.) injection based on body weight measurements. Choice of $MnCl_2$ dosage was based on previously published ME-MRI reports in mice.

Four sets of experimental imaging studies were carried out using individual independent cohorts as outlined below. (i) Temporal change in T_1-enhancement (24 h, 48 h, 72 h, 1 week) of salivary gland tissues in naïve mice ($n = 5$) following systemic $MnCl_2$ administration (0.4 mmol/kg, i.p.), (ii) ME-MR microscopy of salivary gland enhancement in naïve mice ($n = 3$) 24 h post–$MnCl_2$ administration (0.4 mmol/kg $MnCl_2$, i.p.), (iii) comparative assessment of T_1-enhancement of salivary glands in naïve mice 24 h after $MnCl_2$ administration at 0.2 mmol/kg or 0.4 mmol/kg ($n = 5$ per group), and (iv) evaluation of T_1-enhancement of orthotopic ($n = 8$) and ectopic ($n = 6$) HNSCC xenografts 24 h post–$MnCl_2$ administration (0.2 mmol/kg $MnCl_2$, i.p.).

MRI

Imaging studies were carried out using a 4.7-T/33-cm horizontal-bore magnet (GE NMR Instruments, Fremont, CA) incorporating AVANCE digital electronics (Bruker Biospec, ParaVision 3.1; Bruker Medical, Billerica, MA), a removable gradient coil insert (G060;

Bruker Medical) generating a maximum field strength of 950 mT/m, and a custom-designed 35 mm radiofrequency transmit/receive coil. Inhalational anesthesia using isoflurane (Abbott Laboratories, Abbott Park, IL) was utilized to induce (3–4%) and maintain anesthesia (2–2.5%) during imaging procedures. An MR-compatible sled (Dazai Research Instruments, Toronto, Canada) equipped with temperature and respiratory sensors was utilized for positioning of animals and to provide feedback control during imaging. Body temperature of animals was maintained using an air heater system (SA Instruments Inc., Stony Brook, NY).

Three-dimensional T_1-weighted spoiled gradient echo was used with the following parameters: matrix dimensions 192 × 128 × 128; echo time/pulse repetition time = 3.0/15.0 ms, field of view 4.8 × 3.2 × 3.2 cm, number of averages = 1, flip angle 40°, acquisition time 4 min 5 sec. Measurement of T_1-relaxation rates was performed using a saturation recovery fast spin echo with variable repetition times (matrix size 128 × 96, pulse repetition time = 360–6000 ms, echo time/echo time$_{eff}$ = 10/25 ms, 3.2 × 3.2 field of view, five slices, acquisition time 4 min 50 sec), as described previously (12). For ME-MR microscopy, T_1-weighted three-dimensional data sets (echo time/pulse repetition time = 3.0/15.0 ms, flip angle 25°, field of view 4.8 × 2.8 × 2.8, matrix 256 × 150 × 150 matrix, 10 averages, acquisition time 56 min 15 sec) were acquired postmortem. T_1-weighted MR data sets of animals bearing ectopic or orthotopic HNSCC xenografts were acquired using the following parameters: matrix size 128 × 128; echo time/pulse repetition time, 7.0/600 ms; 1 mm slice thickness, field of view, 4.8 × 3.2 cm; number of slices, 21; number of averages, four; acquisition time, 5 min 14 sec.

Following image acquisition, raw image sets were transferred to a processing workstation and converted into Analyze™ format (AnalyzeDirect, version 8.0; Overland Park, KS). Regions of interest were manually traced on anatomic images and transferred to R_1 maps ($R_1 = 1/T_1$) to allow accurate placement. In addition to salivary gland and tumor tissues, murine muscle and the contrast agent phantom were sampled on the images and used to normalize signal intensity values. T_1 (or R_1 values) were calculated for the whole tumor or salivary gland tissues. R_1 maps were calculated on a pixel-by-pixel basis using MatLab (version 7.0; MathWorks Inc., Natick, MA). Statistical analysis was performed using GraphPad Prism (version 5.00 for Windows; GraphPad Software, San Diego, CA). All measured values are reported as mean ± standard deviation of the mean. Statistical significance was set at $P < 0.05$. One-way analysis of variance with Bonferroni's multiple comparisons was used to analyze differences in T_1 values of salivary gland tissues at different times post–$MnCl_2$ administration. Differences in R_1 values of salivary glands and tumor tissues before and after $MnCl_2$ administration were evaluated using two-tailed t test.

RESULTS

To examine the temporal evolution of salivary gland enhancement in mice following systemic administration of Mn^{2+}, naïve athymic nude mice ($n = 5$) were injected with a single dose of $MnCl_2$ (0.4 mmol/kg, i.p.). T_1-weighted MRI was performed at baseline (before administration of $MnCl_2$) and at different times postinjection (24 h, 48 h, 72 h, and 1 week). Systemic administration of $MnCl_2$ resulted in significant enhancement of anatomic contrast in naïve mice. Figure 1 shows the temporal change in enhancement of salivary

gland tissue (arrows) post–$MnCl_2$ administration. Marked signal enhancement of salivary gland tissues was observed 24 h after i.p. administration of $MnCl_2$, which persisted at 48–72 h postinjection (Fig. 1a). T_1 values (mean ± standard deviation, msec) of salivary glands were 1275 ± 81 (baseline), 656.6 ± 283.5 (24 h), 812 ± 234.6 (48 h), 954.1 ± 243.1 (72 h), and 974.8 ± 190.5 (1 week). Significant decrease in T_1 values of salivary glands was observed at the 24 h ($P < 0.01$) and 48 h ($P < 0.05$) time points compared to baseline precontrast T_1 measurements (Fig. 1b). ME-MR microscopy was performed postmortem on a subset of mice ($n = 3$), 24 h post–$MnCl_2$ administration to examine the distribution and selectivity of salivary gland enhancement. As shown in Fig. 2, ME-MR microscopy provided high-resolution three-dimensional images that confirmed the selective enhancement of salivary gland tissue (arrows). Salivary glands appeared markedly enhanced compared to surrounding structures in the neck and enabled accurate delineation of superficial cervical lymph nodes.

To determine the effect of the administered Mn^{2+} dose on salivary gland enhancement, $MnCl_2$ was administered at a dose of 0.4 mmol/kg or 0.2 mmol/kg ($n = 5$ per group) to naïve mice and T_1-relaxation rates were measured 24 h postadministration. The influence of administered Mn dose on contrast enhancement was also visualized by R_1 maps calculated on a pixel-by-pixel basis. As shown in Fig. 3a, R_1 maps revealed marked enhancement of salivary gland tissue 24 h postinjection at 0.4 mmol/kg and 0.2 mmol/kg doses. Both doses of $MnCl_2$ resulted in a statistically significant increase in R_1 of salivary glands (Fig. 3b) compared to precontrast estimates. However, R_1 values measured 24 h postcontrast were not significantly different between the two doses. Therefore, all subsequent studies were performed using the lower dose (0.2 mmol/kg).

To determine enhancement of tumor tissues following $MnCl_2$ administration, nude mice bearing orthotopic and ectopic HNSCC xenografts were utilized. Figure 4a shows T_1-weighted images (normalized to muscle) of ectopic and orthotopic HNSCC xenografts in nude mice before and 24 h after $MnCl_2$ injection at a dose of 0.2 mmol/kg. Both ectopic and orthotopic HNSCC xenografts (Fig. 4b and 4c) showed a statistically significant increase in R_1 values at the 24 h time point compared to baseline measurements ($P < 0.05$). However, the degree of enhancement was considerably lower compared to salivary gland tissue. Interestingly, R_1 values of salivary gland tissues in mice bearing orthotopic HNSCC xenografts were lower compared to naïve animals both before (0.6113 ± 0.07 versus 0.7623 ± 0.07, $P < 0.05$) and 24 h after $MnCl_2$ administration (0.9523 ± 0.25 versus 1.598 ± 0.14, $P < 0.01$).

DISCUSSION

Clinical assessment of salivary gland pathology often involves a combination of physical examination (palpation), transoral or endoscopic visualization, and imaging (13). Although the appropriate method of choice for imaging salivary glands is dictated by the clinical presentation, CT is often used for evaluation of salivary gland pathology (13). MRI techniques are also utilized to examine infiltrative neoplasms of salivary glands and for sialographic studies (13). Specifically, T_1-weighted MRI provides excellent contrast for visualization of tumor margins, perineural spread, and bone invasion and is used in clinical

studies (13 and references within). In the present study, ME-MRI was successfully applied for mapping salivary gland tissues in mice. Selective T_1 enhancement of healthy murine salivary glands was observed in vivo 24 h after systemic administration of $MnCl_2$. Three-dimensional data sets enabled visualization of salivary gland enhancement after systemic administration of $MnCl_2$ at higher resolution, with clear anatomic delineation of tissues in the head and neck region. Ectopic and orthotopic human head and neck carcinoma xenografts also showed enhancement after $MnCl_2$ injection. The results of our study highlight the potential utility of ME-MRI in examining tumors of the head and neck region while simultaneously allowing imaging of normal salivary gland tissues.

Manganese is an essential trace mineral that is important for aerobic energy production (14). It is localized primarily in metabolically active, mitochondria-rich tissues, including liver, kidneys, pancreas, adrenal glands, heart, brain, salivary glands, gastrointestinal mucosa, uterus, and some tumors (14,15). The manganese ion is involved in the regulation of multiple biologic processes, including free radical detoxification, and binds to biologic molecules such as proteins and nucleic acids through calcium and magnesium binding sites (2,5). Mn^{2+} acts as a calcium analog and a competitor for cellular processes that involve calcium, such as exocytosis of secretory vesicles (2,14,15). Although the mechanisms involved in the underlying salivary gland uptake of $MnCl_2$ are unclear, two salivary gland characteristics are likely to be involved, (i) the abundance of mitochondria, and (ii) calcium-mediated signaling (16). Protein synthesis of digestive enzymes is a major salivary gland tissue process and involves many mitochondria, all containing manganese (17). Salivary gland acinar cells are known to carry a subpopulation of mitochondria localized at the plasma membrane (18). Once digestive enzymes are synthesized, they are stored in vesicles within the acinar cells until the autonomic nervous system signals their release via exocytosis (19). This event occurs through calcium-mediated signaling. Calcium influxes into the cell via voltage-gated channels, causing the release of intracellular stores of calcium, which trigger a signaling cascade that allows the vesicles to exocytose their content (18). Since the manganese ion acts as a surrogate marker for calcium, these cells likely absorb manganese (14). The secretory vesicles themselves are thought to store calcium, and these vesicles take up 30% and 55% of the cytosolic space of rat parotid and submandibular glands, respectively (19). In addition, manganese may replace other divalent cations found in salivary gland tissue, such as zinc, which is found in several enzymes, including carbonic anhydrase, carboxypeptidase, and RNA polymerase (20).

One of the concerns with the use of manganese as a contrast agent has been its neuro- and cardiotoxicity (21). Overexposure to manganese has been associated with neurodegenerative, Parkinson-like symptoms in animals and humans (21). This is believed to be related to the interaction between manganese and iron, which alters iron concentrations in the blood and cerebrospinal fluid. Manganese is also cardiotoxic at high concentrations and results in blockade of calcium channels involved in muscle contraction. However, manganese administered in the form of $MnCl_2$ was associated with only minor cardiac symptoms such as vasodilation or increased heart rate, reported with $MnCl_2$ in dogs (21). In contrast to chelated forms such as Mn-DPDP, $MnCl_2$ yields excellent contrast and is safe at low doses (14,21). In our study, we did not observe any lethality with $MnCl_2$ administration. While animals exhibited signs of lethargy during the initial 1-h period postinjection,

complete recovery and normal activity were subsequently observed. The data presented in this paper would argue that $MnCl_2$ could potentially allow for more accurate visualization of salivary gland tissue than Gd-based contrast agents at well-tolerated doses.

We also observed an increase in the T_1-relaxation rate of ectopic and orthotopic tumors after $MnCl_2$ injection. Similar observations have been made in pituitary adenomas and human choroidal melanoma xenografts (7,22). The increased uptake of manganese by tumor cells is believed to be related to their mitotic activity (22). One would therefore anticipate differential uptake of manganese between rapidly growing tumors associated with increased mitotic activity and aerobic respiration through mitochondria compared to slowly growing tumors that use anaerobic glycolysis for energy production (7,22). In the present study, an orthotopic HNSCC tumor model was utilized to enable simultaneous visualization of tumor and salivary gland tissues. Although tumor enhancement was minimal compared to enhancement of salivary gland tissue after manganese administration, significant differences in R_1 values of salivary glands were observed between naïve mice and animals bearing orthotopic HNSCC tumors. The exact cause of this decreased enhancement is unclear. However, if the rate of uptake of Mn^{2+} is considered to be an indicator of normal salivary gland activity, it could be speculated that potential metastatic invasion from the orthotopic HNSCC tumor resulted in the disruption of glandular structure and salivary gland function. In the absence of normal cellular activity within the salivary gland tissue, calcium transport and signaling could be affected, resulting in the decreased uptake of manganese. Similar observations have been reported in the literature (11,22). A differential enhancement was seen following $MnCl_2$ administration between normal and ischemic canine myocardial tissues (11). In rats with retinal tumors, alterations in structure and function were observed in neighboring retinal tissue (22).

In conclusion, we have demonstrated the utility of ME-MRI of imaging of salivary gland tissues and head and neck tumors in living subjects. The findings of our study have useful clinical implications. First, ME-MRI can potentially be applied for examination of neoplastic and nonneoplastic inflammatory diseases of salivary glands when manganese is administered judiciously in doses clinically proven to cause little or no cardiac and neurotoxicity. Indeed, studies have demonstrated that Mn-based contrast agents can be safely used for diagnosis of hepatic lesions and bile duct leaks for MR cholangiopancreatography (23,24). Second, given that maximal contrast enhancement of salivary gland tissues was observed at 24 h after $MnCl_2$ administration, perhaps delayed imaging could be considered for clinical ME-MRI studies. Additional diagnostic utility of delayed MR imaging has been previously suggested with Mn-containing contrast agents for clinical liver imaging (24). Third, the ability of ME-MRI to monitor tumor and normal tissues using ME-MRI is particularly relevant in head and neck oncology. For example, noninvasive imaging of salivary gland function could provide useful insight into the effects of radiation therapy in vivo. Mucositis and xerostomia are two of the major side effects associated with radiation-induced damage to the salivary glands. Therefore, ME-MRI could be utilized for early evaluation of radiation-induced damage to salivary glands in head and neck cancer patients. However, further preclinical investigation into the potential of ME-MRI in monitoring radiation therapy is warranted. Nevertheless, to the best of our knowledge, this is the first

report of a systematic investigation into the application of ME-MRI for imaging of salivary glands and head and neck tumors.

Acknowledgments

Grant sponsors: Roswell Park Alliance Foundation and NCI-Comprehensive Cancer Center Support; Grant number: P30 CA016056-33.

The authors thank Steve Turowski, MS, for his excellent technical assistance and Joseph Spernyak, PhD, for his assistance in developing the imaging protocols and for useful discussions.

References

1. Lauterbur, PC., Mendonca-Dias, M., Rudin, A. Augmentation of tissue water proton spin-lattice relaxation rates by in vivo addition of paramagnetic ions. In: Dutton, P.Leigh, JS., Scarpa, A., editors. Frontiers of Biological Energetics. Academic Press; New York: 1978. p. 752-759.
2. Koretsky AP, Silva AC. Manganese-enhanced magnetic resonance imaging (MEMRI). NMR Biomed. 2004; 17:527–531. [PubMed: 15617051]
3. Kang YS, Gore JC. Studies of tissue NMR relaxation enhancement by manganese: dose and time dependences. Invest Radiol. 1984; 19:399–407. [PubMed: 6511248]
4. Fabry ME, Eisenstadt M. Water exchange between red cells and plasma: measurement by nuclear magnetic relaxation. Biophys J. 1975; 15:1101–1110. [PubMed: 1201327]
5. Silva AC, Lee JH, Aoki I, Koretsky AP. Manganese-enhanced magnetic resonance imaging (MEMRI): methodological and practical considerations. NMR Biomed. 2004; 17:532–543. [PubMed: 15617052]
6. Lee JH, Silva AC, Merkle H, Koretsky AP. Manganese-enhanced magnetic resonance imaging of mouse brain after systemic administration of $MnCl_2$: dose-dependent and temporal evolution of T1 contrast. Magn Reson Med. 2005; 53:640–648. [PubMed: 15723400]
7. Cross DJ, Flexman JA, Anzai Y, Sasaki T, Treuting PM, Maravilla KR, Minoshima S. In vivo manganese MR imaging of calcium influx in spontaneous rat pituitary adenoma. AJNR Am J Neuroradiol. 2007; 28:1865–1871. [PubMed: 17925377]
8. Yu X, Wadghiri YZ, Sanes DH, Turnbull DH. In vivo auditory brain mapping in mice with Mn-enhanced MRI. Nat Neurosci. 2005; 8:961–968. [PubMed: 15924136]
9. Pautler RG, Silva AC, Koretsky AP. In vivo neuronal tract tracing using manganese-enhanced magnetic resonance imaging. Magn Reson Med. 1998; 40:740–748. [PubMed: 9797158]
10. Watanabe T, Frahm J, Michaelis T. Manganese-enhanced MRI of the mouse auditory pathway. Magn Reson Med. 2008; 60:210–212. [PubMed: 18581385]
11. Hu TC, Christian TF, Aletras AH, Taylor JL, Koretsky AP, Arai AE. Manganese enhanced magnetic resonance imaging of normal and ischemic canine heart. Magn Reson Med. 2005; 54:196–200. [PubMed: 15968667]
12. Seshadri M, Toth K. Acute vascular disruption by 5,6-dimethylxanthenone-4-acetic acid in an orthotopic model of human head and neck cancer. Transl Oncol. 2009; 2:121–127. [PubMed: 19701496]
13. Yousem DM, Kraut MA, Chalian AA. Major salivary gland imaging. Radiology. 2000; 216:19–29. [PubMed: 10887223]
14. Wendland MF. Applications of manganese-enhanced magnetic resonance imaging (MEMRI) to imaging of the heart. NMR Biomed. 2004; 17:581–594. [PubMed: 15761947]
15. Oksendal AN, Hals PA. Biodistribution and toxicity of MR imaging contrast media. J Magn Reson Imaging. 1993; 3:157–165. [PubMed: 8428083]
16. Terman BI, Gunter TE. Characterization of the submandibular gland microsomal calcium transport system. Biochim Biophys Acta. 1983; 730:151–160. [PubMed: 6187361]
17. Warner JD, Peters CG, Saunders R, Won JH, Betzenhauser MJ, Gunning WT 3rd, Yule DI, Giovannucci DR. Visualizing form and function in organotypic slices of the adult mouse parotid gland. Am J Physiol Gastrointest Liver Physiol. 2008; 295:G629–640. [PubMed: 18669626]

18. Won JH, Yule DI. Measurement of Ca^{2+} signaling dynamics in exocrine cells with total internal reflection microscopy. Am J Physiol Gastrointest Liver Physiol. 2006; 291:G146–155. [PubMed: 16484681]
19. Martinez JR, Willis S, Puente S, Wells J, Helmke R, Zhang GH. Evidence for a Ca^{2+} pool associated with secretory granules in rat submandibular acinar cells. Biochem J. 1996; 320:627–634. [PubMed: 8973577]
20. Shatzman AR, Henkin RI. Metal-binding characteristics of the parotid salivary protein gustin. Biochim Biophys Acta. 1980; 623:107–118. [PubMed: 7378466]
21. Crossgrove J, Zheng W. Manganese toxicity upon overexposure. NMR Biomed. 2004; 17:544–553. [PubMed: 15617053]
22. Braun RD, Gradianu M, Vistisen KS, Roberts RL, Berkowitz BA. Manganese-enhanced MRI of human choroidal melanoma xenografts. Invest Ophthalmol Vis Sci. 2007; 48:963–967. [PubMed: 17325133]
23. Regge D, Cirillo S, Macera A, Galatola G. Mangafodipir trisodium: review of its use as an injectable contrast medium for magnetic resonance imaging. Rep Med Imaging. 2009; 2:55–68.
24. Chung JJ, Kim MJ, Kim KW. Mangafodipir trisodium-enhanced MRI for the detection and characterization of focal hepatic lesions: is delayed imaging useful? J Magn Reson Imaging. 2006; 23:706–711. [PubMed: 16565954]

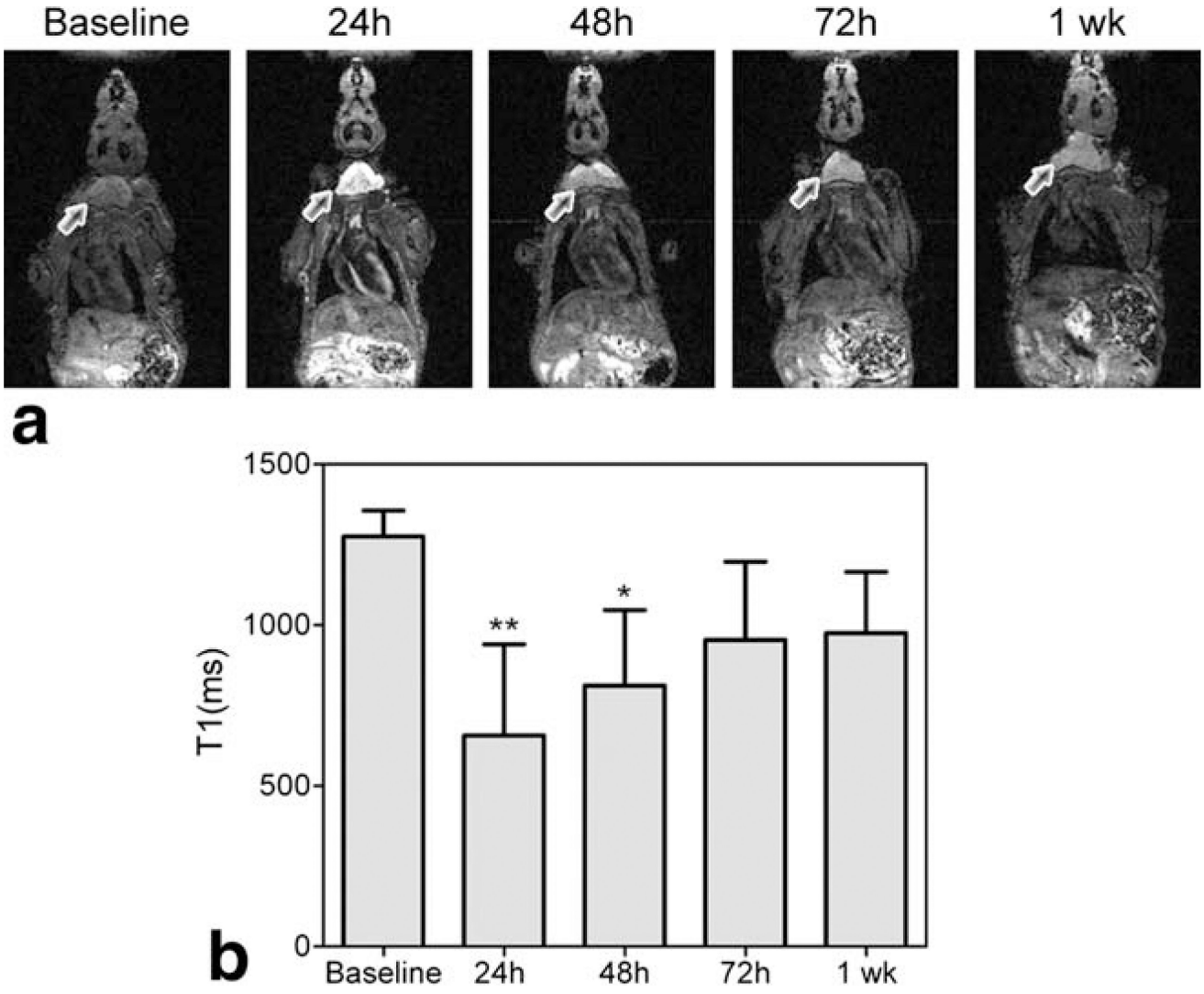

FIG. 1.

Temporary changes in T_1 enhancement of salivary gland tissue (indicated by arrows) in a naïve nude mouse **(a)**. Bar graph shows the T_1-values of salivary glands (indicated by arrows) before and at different times after systemic administration of $MnCl_2$ **(b)**. Data are reported as mean ± standard deviation $^{**}P < 0.01$; $^{*}P < 0.05$.

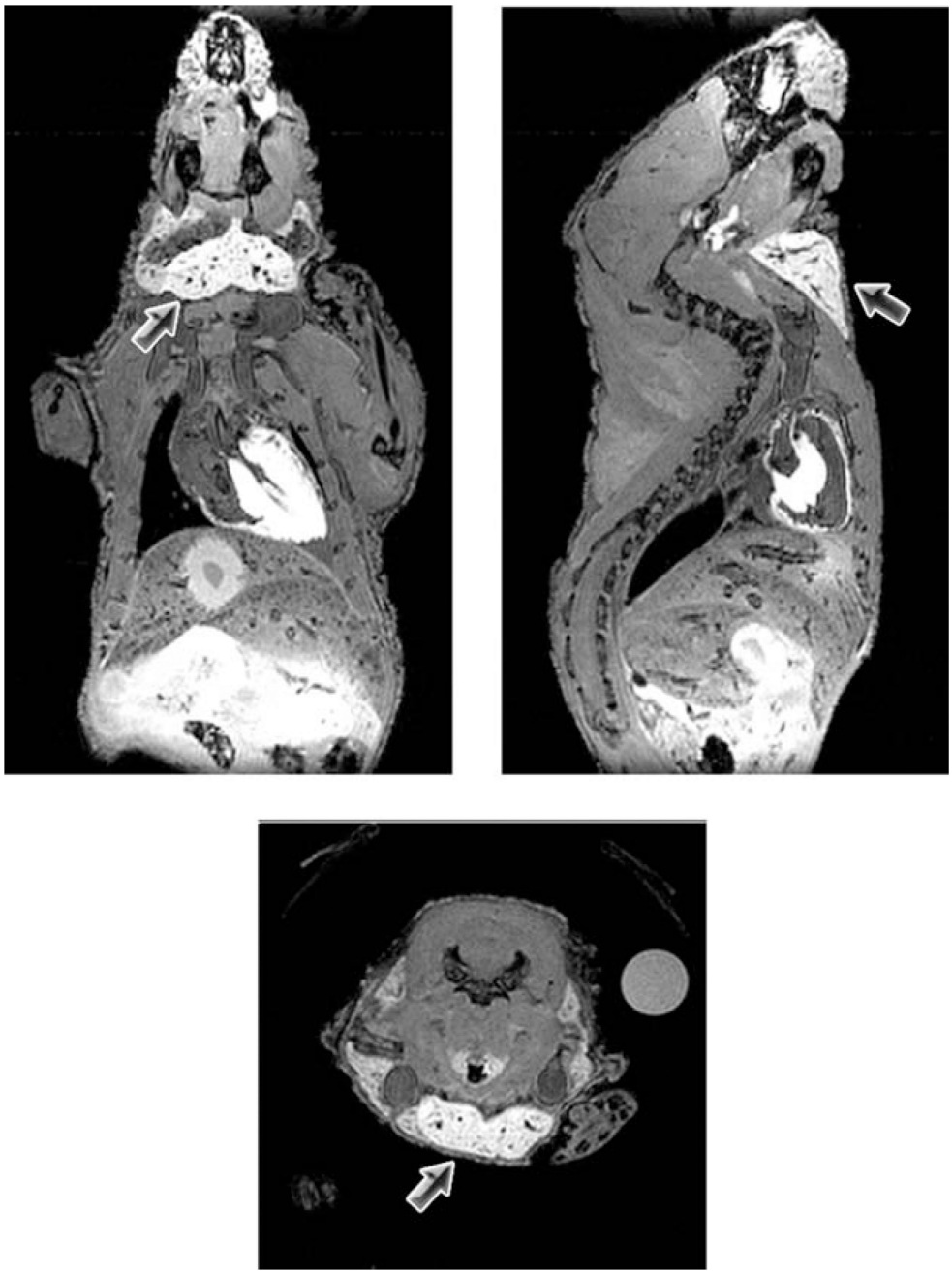

FIG. 2.

ME-MR microscopy of salivary glands 24 h after $MnCl_2$. Coronal, sagittal, and axial slices from a three-dimensional data set acquired postmortem in a naïve mouse are shown. High-resolution images confirmed selective enhancement of salivary gland tissue (arrows).

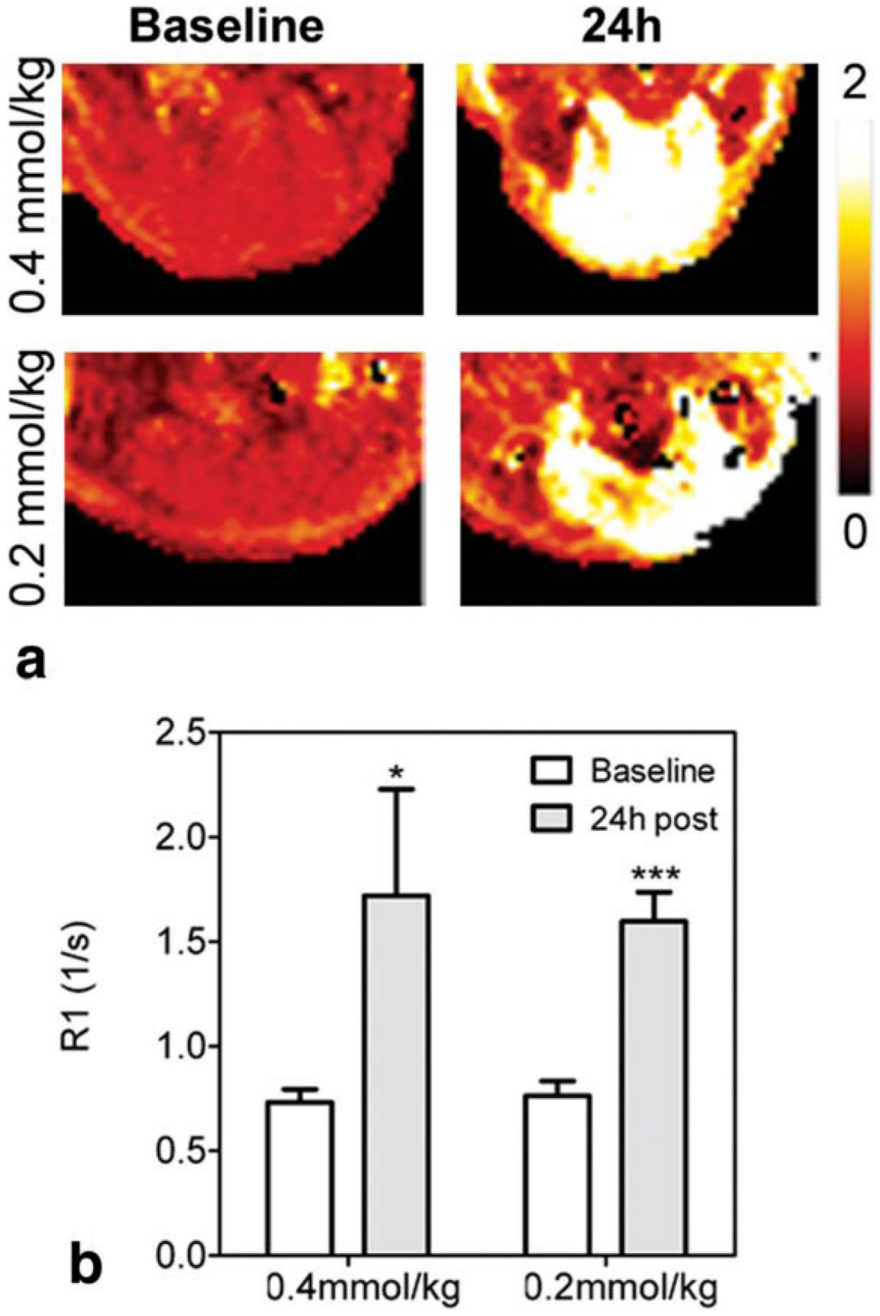

FIG. 3.

Effect of administered Mn^{2+} dose on salivary gland enhancement. Example R_1 maps of naïve mice at baseline and 24 h after $MnCl_2$ administration at a dose of 0.2 or 0.4 mmol/kg **(a)**. Corresponding R_1 values of whole salivary gland regions of interest are also shown **(b)**. Data are reported as mean ± standard deviation. ***$P < 0.001$; *$P < 0.05$.

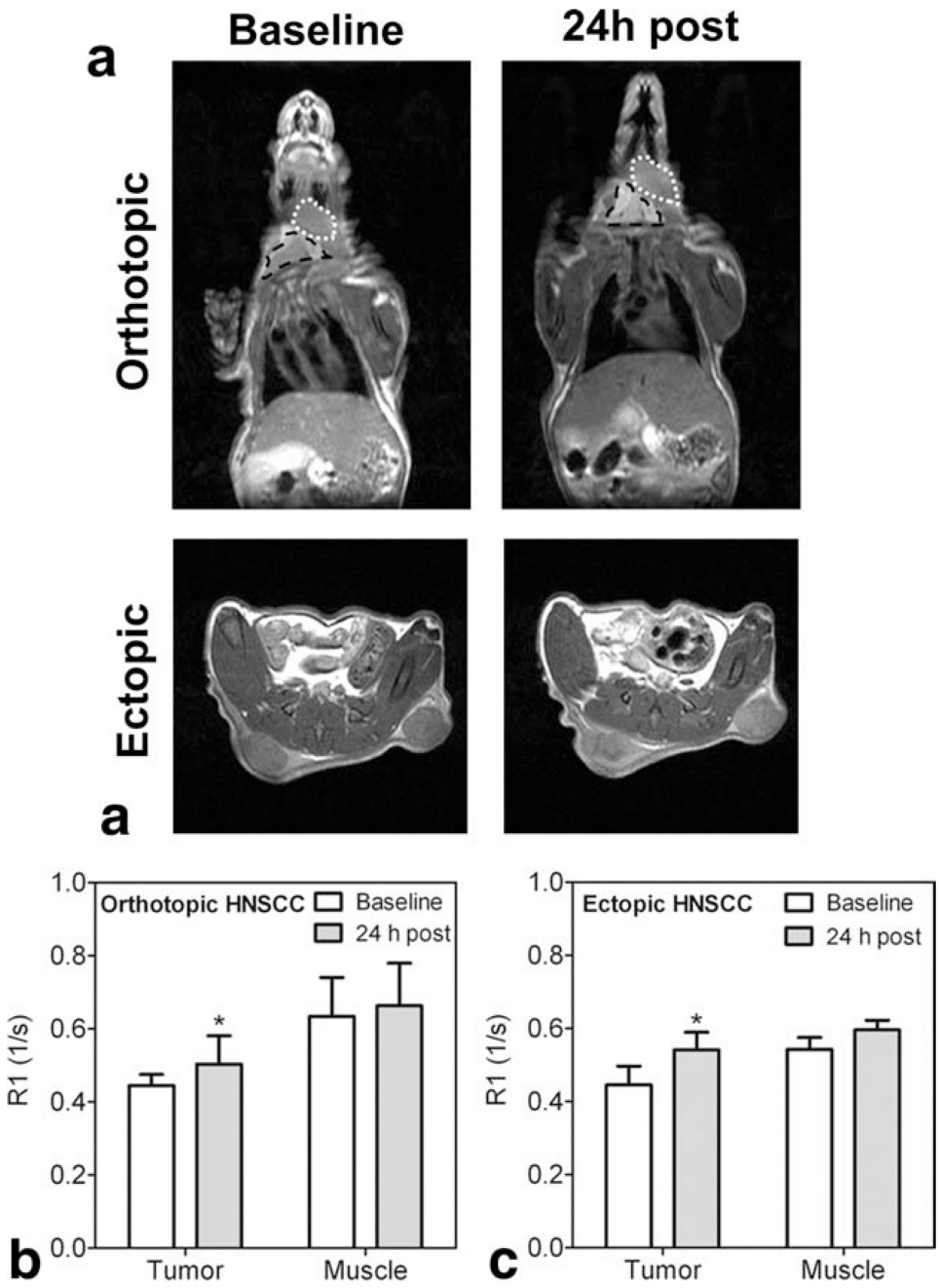

FIG. 4.

ME-MRI of ectopic and orthotopic HNSCC xenografts. Coronal and axial T_1-weighted images of tumor-bearing mice **(a)**. Anatomic extent of tumor (white dotted line) and salivary gland (black outline) are shown in the upper panel of images. R_1 values of whole tumor regions of interest and murine muscle tissue at baseline and 24 h after $MnCl_2$ are also shown for orthotopic **(b)** and ectopic tumors **(c)**. Data are reported as mean ± standard deviation. $*P < 0.05$.